Field-Based-Stabilized Combined Tangential Formulation for the Accurate Solution of Scattering Problems Involving Low-Contrast Dielectric Objects

Özgür Ergül[1,2] **and Levent Gürel**[1,2]
[1]Department of Electrical and Electronics Engineering
[2]Computational Electromagnetics Research Center (BiLCEM)
Bilkent University, TR-06800, Bilkent, Ankara, Turkey
E-mail: ergul@ee.bilkent.edu.tr, lgurel@bilkent.edu.tr

Abstract — We present a robust stabilization technique, which enables the accurate solution of scattering problems involving dielectric objects with arbitrarily low contrasts via surface integral equations (SIEs). Conventional SIEs provide inaccurate results for the scattered fields when the contrast of an object is low, i.e., when the electromagnetic material parameters of the scatterer and the host medium are close to each other. The proposed technique is based on decomposing the equivalent currents into radiating and nonradiating parts, and extracting the dominant nonradiating currents. In addition, we rearrange the right-hand side of the equations by introducing fictitious incident fields to eliminate numerical problems for very low contrasts. The overall stabilization procedure is applied to a combined tangential formulation (CTF) with a negligible computational cost. We show that the resulting stable formulation, which is called the field-based stabilized CTF (FBS-CTF), provides accurate results even for extremely low-contrast objects, and its accuracy does not break down with finite-precision methods, such as the multilevel fast multipole algorithm.

1. INTRODUCTION

Surface integral equations (SIEs) are commonly used to formulate scattering problems involving three-dimensional dielectric objects with arbitrary shapes. Using equivalent electric and magnetic currents and applying the boundary conditions on the surface of the scatterer, a set of integral equations can be obtained. In the literature, various SIE formulations are derived by using diverse combinations of the boundary conditions, testing schemes, and scaling operations for the numerical solution of scattering problems [1]–[15]. Some of these formulations are stable and free of the internal-resonance problem, and they provide accurate results for dielectric objects with moderate dielectric parameters. Unfortunately, those formulations become inaccurate as the contrast of the object decreases, i.e., when the electromagnetic material properties of the object and the host medium become close to each other.

There are various applications that involve scattering from low-contrast objects, such as red blood cells in blood plasma [11],[16],[17], plastic mines buried in soil [18], polymeric materials [19], and dielectric photonic crystals [20]. When the contrast is low, however, traditional SIE formulations encounter stability problems, and the scattered fields cannot be calculated accurately with them. Those scattering problems can be solved accurately with volume integral equations (VIEs) [21], which are stable when the contrast is low. On the other hand, it is also desirable to extend the applicability of SIEs to low-contrast problems in order to use the advantages of the surface formulations, which are usually discretized with fewer unknowns compared to volume formulations.

This work was supported by the Scientific and Technical Research Council of Turkey (TUBITAK) under Research Grant 105E172, by the Turkish Academy of Sciences in the framework of the Young Scientist Award Program (LG/TUBA-GEBIP/2002-1-12), and by contracts from ASELSAN and SSM.

In this paper, we present a robust stabilization technique, which enables the accurate solution of low-contrast problems with SIEs. This technique is based on decomposing the equivalent currents into radiating and nonradiating parts [22],[23]. The nonradiating currents correspond to the tangential incident fields on the surface of the scatterer. When the contrast of the object is low, the nonradiating currents dominate the solution, and the radiating currents form very small portions of the total currents. Therefore, when the total currents are solved by employing the conventional surface formulations, it becomes difficult to perform the calculations accurately enough to capture the small radiating currents properly. By extracting the nonradiating currents, however, the radiating currents can be computed accurately even for low-contrast objects, i.e., when the radiating currents are numerically insignificant compared to the nonradiating currents.

Extraction of the nonradiating currents is necessary but not sufficient to solve problems with arbitrarily low contrasts. Numerical errors arising on the right-hand sides (RHSs) of integral equations become significant and deteriorate the accuracy of the results when the contrast decreases to very low values. As a remedy, we define fictitious incident fields and rearrange the RHSs of the equations. The overall stabilization procedure, which involves the extraction of the nonradiating currents and the rearrangement of the RHS, is applied to a combined tangential formulation (CTF). We show that the resulting stable formulation, which we call the field-based stabilized CTF (FBS-CTF), provides accurate results even for extremely low-contrast objects. FBS-CTF is easy to implement by modifying the existing codes for the conventional CTF, it has a negligible extra cost, and its accuracy does not break down with finite-precision methods, such as the fast multipole method [24] and the multilevel fast multipole algorithm (MLFMA) [25].

2. SURFACE INTEGRAL EQUATIONS

For homogenous dielectric objects, SIE formulations are constructed by combining tangential (T) and normal equations (N), namely, the tangential electric-field integral equation (T-EFIE), the normal electric-field integral equation (N-EFIE), the tangential magnetic-field integral equation (T-MFIE), and the normal magnetic-field integral equation (N-MFIE) [8]. In the T equations, boundary conditions are tested directly by sampling the tangential components of the electric and magnetic fields on the surface. In the N equations, however, electromagnetic fields are tested after they are projected onto the surface via a cross-product operation with the outward normal vector $\hat{\boldsymbol{n}}$. These equations can be obtained for both the inner and outer regions, and they can be combined in diverse ways to derive various SIE formulations [1]–[15].

In general, SIE formulations can be categorized into three groups, i.e., tangential, normal, and mixed formulations, depending on the integral equations used to construct the formulation. The tangential formulations, such as the tangential Poggio-Miller-Chang-Harrington-Wu-Tsai (T-PMCHWT) formulation [2]–[4] and CTF [13], are obtained by using T-EFIE and T-MFIE. In both formulations, T-EFIE and T-MFIE are solved simultaneously, while the inner and outer equations are linearly combined to avoid internal resonances. Similar combinations of N-EFIE and N-MFIE lead to the normal formulations, such as the combined normal formulation (CNF) [13], the normal Müller formulation (NMF) [1], and the modified normal Müller formulation (MNMF) [14]. Finally, the mixed formulations, such as the electric and magnetic current combined-field integral equation (JMCFIE) [12],[26] and the combined PMCHWT Müller formulation (CPMF) [27], are obtained by combining the tangential and normal formulations appropriately. JMCFIE involves a combination of CTF and CNF, while CPMF is a similar combination of PMCHWT and MNMF. There are also other types of mixed formulations, which are generally called the combined-field integral equation (CFIE) formulations, where the T-EFIE, T-MFIE, N-EFIE, and N-MFIE are combined in various ways while the inner and outer problems are solved simultaneously [7]–[10].

Using a Galerkin scheme in the discretization of the surface formulations, i.e., using the same set of functions to expand the current densities (basis functions) and to test the boundary conditions (testing

functions), the normal and mixed formulations contain well-tested identity operators [13]. Therefore, these formulations usually produce well-conditioned matrix equations, which are easy to solve iteratively. However, the tangential formulations do not contain well-tested identity operators, and their discretizations may lead to ill-conditioned matrix equations. For the efficiency of the solutions, normal and mixed formulations are preferable, especially when problems involve large objects discretized with large numbers of unknowns [28],[29]. On the other hand, errors in the discretization of the well-tested identity operators may deteriorate the accuracy of the solutions obtained with the normal and mixed formulations [13]. The excessive error in those formulations compared to the tangential formulations can be significant [27],[28],[29], especially in conventional implementations employing the low-order Rao-Wilton-Glisson (RWG) functions [30]. In such cases, it is helpful to improve the discretizations either by employing higher-order basis functions [13],[31] or by reducing the size of the discretization elements, to obtain accurate results.

Conventional SIE formulations are stable and provide accurate solutions (with various levels of accuracy, depending on the existence of well-tested identity operators, types of the basis and testing functions, discretization method, geometry of the object, etc.), for problems involving objects with moderate contrasts. However, those formulations become inaccurate to calculate the scattered fields as the contrast of the object decreases, i.e., when the electromagnetic material properties of the object and the host medium become close to each other. This is one of the major drawbacks of the SIE formulations in comparison to VIE formulations, which do not break down for low contrasts. In this paper, we present a robust stabilization procedure to eliminate the low-contrast breakdown in surface formulations.

3. COMBINED TANGENTIAL FORMULATION

The stabilization procedure is applied to CTF (that is slightly different from the original CTF presented in [13]), although it can be generalized to other existing formulations in the literature. Consider scattering from a homogenous dielectric object with a three-dimensional arbitrary shape. We assume time-harmonic electromagnetic fields with $e^{-i\omega t}$ time dependence. Incident electromagnetic fields are created by some external sources located outside the object. To derive CTF, operators for the outside ($l = 0$) and inside ($l = 1$) the object are defined as

$$\mathcal{K}_l\{\boldsymbol{X}\}(\boldsymbol{r}) = \int_{PV,S} d\boldsymbol{r'}\boldsymbol{X}(\boldsymbol{r'}) \times \nabla' g_l(\boldsymbol{r},\boldsymbol{r'}) \tag{1}$$

$$\mathcal{T}_l\{\boldsymbol{X}\}(\boldsymbol{r}) = ik_l \int_S d\boldsymbol{r'}\Big[\boldsymbol{X}(\boldsymbol{r'}) + \frac{1}{k_l^2}\nabla' \cdot \boldsymbol{X}(\boldsymbol{r'})\nabla\Big] g_l(\boldsymbol{r},\boldsymbol{r'}), \tag{2}$$

where $\boldsymbol{X}(\boldsymbol{r})$ is either the equivalent electric current $\boldsymbol{J}(\boldsymbol{r}) = \hat{\boldsymbol{n}} \times \boldsymbol{H}(\boldsymbol{r})$ or the equivalent magnetic current $\boldsymbol{M}(\boldsymbol{r}) = -\hat{\boldsymbol{n}} \times \boldsymbol{E}(\boldsymbol{r})$ on the surface of the object S, $k_l = \omega\sqrt{\mu_l \epsilon_l}$ is the wavenumber associated with medium l, and

$$g_l(\boldsymbol{r},\boldsymbol{r'}) = \frac{\exp(ik_l R)}{4\pi R} \qquad \Big(R = |\boldsymbol{r} - \boldsymbol{r'}|\Big) \tag{3}$$

denotes the homogeneous-space Green's function.

CTF is obtained by combining the inner and outer tangential equations, i.e., T-EFIE$_0$ + T-EFIE$_1$ and T-MFIE$_0$ + T-MFIE$_1$, as

$$\hat{\boldsymbol{t}} \cdot \begin{bmatrix} \eta_0\mathcal{T}_0 + \eta_1\mathcal{T}_1 & -\Big(\mathcal{K}_0 + \mathcal{K}_1\Big) \\ \eta_0\eta_1\Big(\mathcal{K}_0 + \mathcal{K}_1\Big) & \eta_1\mathcal{T}_0 + \eta_0\mathcal{T}_1 \end{bmatrix} \cdot \begin{bmatrix} \boldsymbol{J} \\ \boldsymbol{M} \end{bmatrix}(\boldsymbol{r}) = -\hat{\boldsymbol{t}} \cdot \begin{bmatrix} \boldsymbol{E}^i(\boldsymbol{r}) \\ \eta_0\eta_1\boldsymbol{H}^i(\boldsymbol{r}) \end{bmatrix}, \tag{4}$$

where $\boldsymbol{E}^i(\boldsymbol{r})$ and $\boldsymbol{H}^i(\boldsymbol{r})$ are the incident electric and magnetic fields, $\eta_l = \sqrt{\mu_l/\epsilon_l}$ is the impedance of medium l, and $\hat{\boldsymbol{t}}$ is any tangential vector at the observation point $\boldsymbol{r}$ on the surface. CTF in (4) does not contain any identity operator, and $\mathcal{K}$ operators are not well-tested [13],[27]. On the other hand, $\mathcal{T}$

operators are well-tested and they are located in the diagonal blocks. For low contrasts, i.e., $\epsilon_1 \approx \epsilon_0$ and $\mu_1 \approx \mu_0$, the diagonal blocks in (4) are numerically well-balanced, which is a desirable property in terms of conditioning [13].

3.1. Discretization

For numerical solutions of CTF, surface currents are expanded in a series of RWG functions, i.e.,

$$\boldsymbol{J}(\boldsymbol{r}) = \sum_{n=1}^{N} x_n \boldsymbol{b}_n(\boldsymbol{r}) \tag{5}$$

$$\boldsymbol{M}(\boldsymbol{r}) = \sum_{n=1}^{N} y_n \boldsymbol{b}_n(\boldsymbol{r}), \tag{6}$$

where $\boldsymbol{b}_n(\boldsymbol{r})$ for $n = 1, 2, ..., N$ represents the nth basis function with a spatial support of A_n, while x_n and y_n are unknown coefficients. Using a Galerkin scheme, we employ the same set of RWG functions to test the boundary conditions, i.e., $\boldsymbol{t}_m(\boldsymbol{r})$ for $m = 1, 2, ..., N$. Discretization of CTF leads to $2N \times 2N$ dense matrix equations in the form of

$$\begin{bmatrix} \bar{\boldsymbol{Z}}_{11} & \bar{\boldsymbol{Z}}_{12} \\ \bar{\boldsymbol{Z}}_{21} & \bar{\boldsymbol{Z}}_{22} \end{bmatrix} \cdot \begin{bmatrix} \boldsymbol{x} \\ \boldsymbol{y} \end{bmatrix} = - \begin{bmatrix} \boldsymbol{v} \\ \eta_0\eta_1 \boldsymbol{w} \end{bmatrix}, \tag{7}$$

where $\boldsymbol{x}$ and $\boldsymbol{y}$ are column vectors involving the unknown coefficients in (5) and (6), respectively. Matrix elements in (7) are derived as

$$\bar{\boldsymbol{Z}}_{11} = \eta_0 \bar{\boldsymbol{T}}_0 + \eta_1 \bar{\boldsymbol{T}}_1 \tag{8}$$

$$\bar{\boldsymbol{Z}}_{12} = -\bar{\boldsymbol{K}}_0 - \bar{\boldsymbol{K}}_1 \tag{9}$$

$$\bar{\boldsymbol{Z}}_{21} = \eta_0\eta_1 \bar{\boldsymbol{K}}_0 + \eta_0\eta_1 \bar{\boldsymbol{K}}_1 \tag{10}$$

$$\bar{\boldsymbol{Z}}_{22} = \eta_1 \bar{\boldsymbol{T}}_0 + \eta_0 \bar{\boldsymbol{T}}_1, \tag{11}$$

where

$$\bar{\boldsymbol{K}}_l[m,n] = \int_{A_m} d\boldsymbol{r} \boldsymbol{t}_m(\boldsymbol{r}) \cdot \int_{PV,A_n} d\boldsymbol{r'} \boldsymbol{b}_n(\boldsymbol{r'}) \times \nabla' g_l(\boldsymbol{r}, \boldsymbol{r'}) \tag{12}$$

$$\begin{aligned} \bar{\boldsymbol{T}}_l[m,n] = {} & ik_l \int_{A_m} d\boldsymbol{r} \boldsymbol{t}_m(\boldsymbol{r}) \cdot \int_{A_n} d\boldsymbol{r'} \boldsymbol{b}_n(\boldsymbol{r'}) g_l(\boldsymbol{r}, \boldsymbol{r'}) \\ & - \frac{i}{k_l} \int_{A_m} d\boldsymbol{r} \boldsymbol{t}_m(\boldsymbol{r}) \cdot \int_{A_n} d\boldsymbol{r'} \nabla' \cdot \boldsymbol{b}_n(\boldsymbol{r'}) \nabla' g_l(\boldsymbol{r}, \boldsymbol{r'}) \end{aligned} \tag{13}$$

for $m, n = 1, 2, ..., N$, and $l = 0, 1$. As it is commonly practiced in the T-EFIE formulations of perfectly-conducting objects [30], the hyper-singularity in (13) removed by placing the differential operator onto the divergence-conforming testing functions, i.e.,

$$\begin{aligned} \bar{\boldsymbol{T}}_l[m,n] = {} & ik_l \int_{A_m} d\boldsymbol{r} \boldsymbol{t}_m(\boldsymbol{r}) \cdot \int_{A_n} d\boldsymbol{r'} \boldsymbol{b}_n(\boldsymbol{r'}) g_l(\boldsymbol{r}, \boldsymbol{r'}) \\ & + \frac{i}{k_l} \int_{A_m} d\boldsymbol{r} \nabla \cdot \boldsymbol{t}_m(\boldsymbol{r}) \int_{A_n} d\boldsymbol{r'} \nabla' \cdot \boldsymbol{b}_n(\boldsymbol{r'}) g_l(\boldsymbol{r}, \boldsymbol{r'}). \end{aligned} \tag{14}$$

Integrals in (12) and (14) are evaluated accurately by employing Gaussian quadrature rules, adaptive integration methods, and singularity extraction techniques [32]–[37]. Finally, to calculate the elements of the RHS vector in (7), the integrals

$$\boldsymbol{v}[m] = \int_{A_m} d\boldsymbol{r} \boldsymbol{t}_m(\boldsymbol{r}) \cdot \boldsymbol{E}^i(\boldsymbol{r}) \tag{15}$$

$$\boldsymbol{w}[m] = \int_{A_m} d\boldsymbol{r} \boldsymbol{t}_m(\boldsymbol{r}) \cdot \boldsymbol{H}^i(\boldsymbol{r}) \tag{16}$$

are evaluated for $m = 1, 2, ..., N$.

3.2. Solutions via MLFMA

Matrix equations obtained with CTF can be solved iteratively, where the required matrix-vector multiplications are performed efficiently by MLFMA in $\mathcal{O}(N \log N)$ time using $\mathcal{O}(N \log N)$ memory [25]. A tree structure of $\mathcal{O}(\log N)$ levels is constructed by placing the dielectric object in a cubic box and recursively dividing the computational domain into sub-boxes (clusters). Then, MLFMA calculates the distant interactions between the basis and testing functions in a group-by-group manner consisting of three stages called aggregation, translation, and disaggregation [38]. In each matrix-vector multiplication, these stages are performed on the tree structure in a multilevel scheme.

By factorizing the Green's function and performing a diagonalization [24], the matrix elements in (12) and (14) can be rewritten as

$$\bar{\boldsymbol{K}}_l[m,n] = \left(\frac{ik_l}{4\pi}\right)^2 \int d^2\hat{\boldsymbol{k}} \boldsymbol{F}^{\mathcal{K}}_{mC}(\boldsymbol{k}_l)\alpha_{L_l}(\boldsymbol{k}_l, \boldsymbol{R}_{CC'}) \cdot \boldsymbol{S}_{C'n}(\boldsymbol{k}_l) \tag{17}$$

$$\bar{\boldsymbol{T}}_l[m,n] = \left(\frac{ik_l}{4\pi}\right)^2 \int d^2\hat{\boldsymbol{k}} \boldsymbol{F}^{\mathcal{T}}_{mC}(\boldsymbol{k}_l)\alpha_{L_l}(\boldsymbol{k}_l, \boldsymbol{R}_{CC'}) \cdot \boldsymbol{S}_{C'n}(\boldsymbol{k}_l) \tag{18}$$

when the testing and basis functions are far from each other. In (17) and (18), $\hat{\boldsymbol{k}}$ is the angular direction, $\boldsymbol{k}_l = k_l\hat{\boldsymbol{k}}$, and

$$\alpha_{L_l}(\boldsymbol{k}_l, \boldsymbol{R}_{CC'}) = \sum_{t=0}^{L_l} i^t(2t+1)h_t^{(1)}(k_l R_{CC'})P_t(\hat{\boldsymbol{R}}_{CC'} \cdot \hat{\boldsymbol{k}}) \tag{19}$$

is the translation operator expressed in terms of the spherical Hankel function of the first kind $h_t^{(1)}$ and the Legendre polynomial P_t. In (17) and (18), the radiation pattern of the nth basis function in cluster C', i.e., $\boldsymbol{S}_{C'n}(\boldsymbol{k}_l)$, is translated into incoming fields for the testing functions in cluster C. The distance between the clusters is represented by the vector

$$\boldsymbol{R}_{CC'} = R_{CC'}\hat{\boldsymbol{R}}_{CC'} = \boldsymbol{r}_C - \boldsymbol{r}_{C'}, \tag{20}$$

where $\boldsymbol{r}_C$ and $\boldsymbol{r}_{C'}$ are reference points of the clusters C and C', respectively. Then, the incoming fields are received by using the receiving patterns of the mth testing function, i.e., $\boldsymbol{F}^{\mathcal{K}}_{mC}(\boldsymbol{k}_l)$ and $\boldsymbol{F}^{\mathcal{T}}_{mC}(\boldsymbol{k}_l)$. Using a Galerkin scheme, the radiation and receiving patterns are calculated as [8],[29]

$$\boldsymbol{S}_{C'n}(\boldsymbol{k}_l) = \int_{S_n} d\boldsymbol{r'} \exp\left[-i\boldsymbol{k}_l \cdot (\boldsymbol{r'} - \boldsymbol{r}_{C'})\right](\bar{\boldsymbol{I}}_{3\times3} - \hat{\boldsymbol{k}}\hat{\boldsymbol{k}}) \cdot \boldsymbol{b}_n(\boldsymbol{r'}) \tag{21}$$

$$\boldsymbol{F}^{\mathcal{K}}_{mC}(\boldsymbol{k}_l) = -\hat{\boldsymbol{k}} \times \left\{\boldsymbol{S}_{Cm}(\boldsymbol{k}_l)\right\}^* \tag{22}$$

$$\boldsymbol{F}^{\mathcal{T}}_{mC}(\boldsymbol{k}_l) = \left\{\boldsymbol{S}_{Cm}(\boldsymbol{k}_l)\right\}^*, \tag{23}$$

where $\bar{\boldsymbol{I}}_{3\times3}$ denotes the 3×3 unit dyad and "*" represents the complex-conjugate operation.

In MLFMA, the interactions in (17) and (18) are calculated in a multilevel scheme. During the aggregation stage, radiation patterns of the clusters are calculated from the bottom to the top of the tree structure. Then, translations are performed to obtain the incoming fields for all clusters. Finally, the disaggregation stage is performed from the top of the tree structure to the lowest level, where the incoming fields are received by the testing functions to complete the matrix-vector multiplications. For each cluster, radiation and receiving patterns are sampled at $(L_l+1) \times (2L_l+2)$ angular points, where L_l is the truncation number in (19) that is determined by the excess bandwidth formula [39]. Since L_l is proportional to the size of the clusters with respect to the wavelength, different tree structures are constructed for the inner and outer media.

3.3. Low-Contrast Breakdown

Scattered fields obtained by using conventional formulations, such as CTF, become inaccurate as the contrast of the object decreases, i.e., when the electromagnetic material properties of the object and the host medium become close to each other. To explain this breakdown, we note that any arbitrary solution can be decomposed as

$$\boldsymbol{J}(\boldsymbol{r}) = \mathcal{I}^{\times n}\{\boldsymbol{H}\}(\boldsymbol{r}) = \hat{\boldsymbol{n}} \times \boldsymbol{H}(\boldsymbol{r}) = \hat{\boldsymbol{n}} \times \boldsymbol{H}^i(\boldsymbol{r}) + \hat{\boldsymbol{n}} \times \boldsymbol{H}^r(\boldsymbol{r}) \tag{24}$$

$$\boldsymbol{M}(\boldsymbol{r}) = -\mathcal{I}^{\times n}\{\boldsymbol{E}\}(\boldsymbol{r}) = -\hat{\boldsymbol{n}} \times \boldsymbol{E}(\boldsymbol{r}) = -\hat{\boldsymbol{n}} \times \boldsymbol{E}^i(\boldsymbol{r}) - \hat{\boldsymbol{n}} \times \boldsymbol{E}^r(\boldsymbol{r}), \tag{25}$$

where $\{\boldsymbol{J}^i(\boldsymbol{r}),\boldsymbol{M}^i(\boldsymbol{r})\}=\{\hat{\boldsymbol{n}} \times \boldsymbol{H}^i(\boldsymbol{r}), -\hat{\boldsymbol{n}} \times \boldsymbol{E}^i(\boldsymbol{r})\}$ do not radiate, i.e.,

$$\left[\begin{array}{cc} \eta_0\mathcal{T}_0 & -\mathcal{K}_0 + 0.5\mathcal{I}^{\times n} \\ \mathcal{K}_0 - 0.5\mathcal{I}^{\times n} & \eta_0^{-1}\mathcal{T}_0 \end{array} \right] \cdot \left[\begin{array}{c} \boldsymbol{J}^i \\ \boldsymbol{M}^i \end{array} \right](\boldsymbol{r}) = \left[\begin{array}{c} 0 \\ 0 \end{array} \right]. \tag{26}$$

As the contrast goes to zero, the nonradiating currents dominate the total currents, while the radiating currents, i.e., $\{\boldsymbol{J}^r(\boldsymbol{r}),\boldsymbol{M}^r(\boldsymbol{r})\}=\{\hat{\boldsymbol{n}} \times \boldsymbol{H}^r(\boldsymbol{r}), -\hat{\boldsymbol{n}} \times \boldsymbol{E}^r(\boldsymbol{r})\}$, tend to vanish. Therefore, when the total currents are solved by employing the conventional surface formulations, it becomes difficult to perform the calculations accurately enough to capture the small radiating currents properly. The total currents $\boldsymbol{J}(\boldsymbol{r})$ and $\boldsymbol{M}(\boldsymbol{r})$ can be computed with relatively small error, but scattered fields may not be obtained accurately from them [22].

4. STABILIZATION OF CTF

For the accurate solution of scattering problems involving low-contrast objects, CTF is stabilized by extracting the nonradiating currents and solving only the radiating currents [23]. The resulting formulation, which we call stable CTF (S-CTF), can be written as

$$\begin{aligned} \hat{\boldsymbol{t}} \cdot \left[\begin{array}{cc} \eta_0\mathcal{T}_0 + \eta_1\mathcal{T}_1 & -\Big(\mathcal{K}_0 + \mathcal{K}_1\Big) \\ \eta_0\eta_1\Big(\mathcal{K}_0 + \mathcal{K}_1\Big) & \eta_1\mathcal{T}_0 + \eta_0\mathcal{T}_1 \end{array} \right] \cdot \left[\begin{array}{c} \boldsymbol{J}^r \\ \boldsymbol{M}^r \end{array} \right](\boldsymbol{r}) \\ = \hat{\boldsymbol{t}} \cdot \left[\begin{array}{cc} \eta_0\mathcal{T}_0 - \eta_1\mathcal{T}_1 & -\Big(\mathcal{K}_0 - \mathcal{K}_1\Big) \\ \eta_0\eta_1\Big(\mathcal{K}_0 - \mathcal{K}_1\Big) & \eta_1\mathcal{T}_0 - \eta_0\mathcal{T}_1 \end{array} \right] \cdot \left[\begin{array}{c} \boldsymbol{J}^i \\ \boldsymbol{M}^i \end{array} \right](\boldsymbol{r}). \end{aligned} \tag{27}$$

We note that the left-hand side (LHS) of S-CTF in (27) is the same as the LHS of CTF in (4), and the stabilization procedure alters only the RHS of the original formulation. Discretization of (27) leads to

$$\left[\begin{array}{cc} \bar{\boldsymbol{Z}}_{11} & \bar{\boldsymbol{Z}}_{12} \\ \bar{\boldsymbol{Z}}_{21} & \bar{\boldsymbol{Z}}_{22} \end{array} \right] \cdot \left[\begin{array}{c} \boldsymbol{x}^r \\ \boldsymbol{y}^r \end{array} \right] = \left[\begin{array}{cc} \bar{\boldsymbol{Y}}_{11} & \bar{\boldsymbol{Y}}_{12} \\ \bar{\boldsymbol{Y}}_{21} & \bar{\boldsymbol{Y}}_{22} \end{array} \right] \cdot \left[\begin{array}{c} \boldsymbol{x}^i \\ \boldsymbol{y}^i \end{array} \right], \tag{28}$$

where

$$\bar{\boldsymbol{Y}}_{11} = \eta_0\bar{\boldsymbol{T}}_0 - \eta_1\bar{\boldsymbol{T}}_1 \tag{29}$$

$$\bar{\boldsymbol{Y}}_{12} = -\bar{\boldsymbol{K}}_0 + \bar{\boldsymbol{K}}_1 \tag{30}$$

$$\bar{\boldsymbol{Y}}_{21} = \eta_0\eta_1\bar{\boldsymbol{K}}_0 - \eta_0\eta_1\bar{\boldsymbol{K}}_1 \tag{31}$$

$$\bar{\boldsymbol{Y}}_{22} = \eta_1\bar{\boldsymbol{T}}_0 - \eta_0\bar{\boldsymbol{T}}_1. \tag{32}$$

In (28), $\{\boldsymbol{x}^r, \boldsymbol{y}^r\}$ and $\{\boldsymbol{x}^i, \boldsymbol{y}^i\}$ are two sets of column vectors involving the coefficients expanding the radiating and nonradiating currents, respectively, i.e.,

$$\{\hat{\boldsymbol{n}} \times \boldsymbol{H}^r(\boldsymbol{r}), -\hat{\boldsymbol{n}} \times \boldsymbol{E}^r(\boldsymbol{r})\} = \sum_{n=1}^{N} \{x_n^r, y_n^r\}\boldsymbol{b}_n(\boldsymbol{r}) \tag{33}$$

$$\{\hat{\boldsymbol{n}} \times \boldsymbol{H}^i(\boldsymbol{r}), -\hat{\boldsymbol{n}} \times \boldsymbol{E}^i(\boldsymbol{r})\} = \sum_{n=1}^{N} \{x_n^i, y_n^i\}\boldsymbol{b}_n(\boldsymbol{r}). \tag{34}$$

To obtain the coefficients expanding the known nonradiating currents, we solve the sparse matrix equation [23]

$$\left[\begin{array}{cc} \bar{\boldsymbol{I}} & 0 \\ 0 & \bar{\boldsymbol{I}} \end{array}\right] \cdot \left[\begin{array}{c} \boldsymbol{x}^i \\ \boldsymbol{y}^i \end{array}\right] = \left[\begin{array}{c} \boldsymbol{w}^{\times n} \\ -\boldsymbol{v}^{\times n} \end{array}\right], \tag{35}$$

where

$$\bar{\boldsymbol{I}}[m,n] = \int_{A_m} d\boldsymbol{r} \boldsymbol{t}_m(\boldsymbol{r}) \cdot \boldsymbol{b}_n(\boldsymbol{r}) \tag{36}$$

$$\boldsymbol{w}^{\times n} = \int_{A_m} d\boldsymbol{r} \boldsymbol{t}_m(\boldsymbol{r}) \cdot \hat{\boldsymbol{n}} \times \boldsymbol{H}^i(\boldsymbol{r}) \tag{37}$$

$$\boldsymbol{v}^{\times n} = \int_{A_m} d\boldsymbol{r} \boldsymbol{t}_m(\boldsymbol{r}) \cdot \hat{\boldsymbol{n}} \times \boldsymbol{E}^i(\boldsymbol{r}). \tag{38}$$

Inserting (35) in (28), discretized S-CTF can be written as

$$\left[\begin{array}{cc} \bar{\boldsymbol{Z}}_{11} & \bar{\boldsymbol{Z}}_{12} \\ \bar{\boldsymbol{Z}}_{21} & \bar{\boldsymbol{Z}}_{22} \end{array}\right] \cdot \left[\begin{array}{c} \boldsymbol{x}^r \\ \boldsymbol{y}^r \end{array}\right] = \left[\begin{array}{cc} \bar{\boldsymbol{Y}}_{11} & \bar{\boldsymbol{Y}}_{12} \\ \bar{\boldsymbol{Y}}_{21} & \bar{\boldsymbol{Y}}_{22} \end{array}\right] \cdot \left[\begin{array}{cc} \bar{\boldsymbol{I}} & 0 \\ 0 & \bar{\boldsymbol{I}} \end{array}\right]^{-1} \cdot \left[\begin{array}{c} \boldsymbol{w}^{\times n} \\ -\boldsymbol{v}^{\times n} \end{array}\right]. \tag{39}$$

In S-CTF, the nonradiating currents are located on the RHS and only the radiating currents are solved for. This way, the radiating currents can be computed accurately for low-contrast objects, i.e., when the radiating currents are numerically insignificant compared to the nonradiating currents. Despite this corrective approach, even S-CTF breaks down and fails to provide accurate results for very low contrasts. The reason is the numerical errors arising during the computation of the RHS of S-CTF. On the RHS, $\mathcal{K}$ and $\mathcal{T}$ operators are applied on the nonradiating currents via matrix-vector multiplications, i.e.,

$$\left[\begin{array}{cc} \bar{\boldsymbol{Y}}_{11} & \bar{\boldsymbol{Y}}_{12} \\ \bar{\boldsymbol{Y}}_{21} & \bar{\boldsymbol{Y}}_{22} \end{array}\right] \cdot \left[\begin{array}{c} \boldsymbol{x}^i \\ \boldsymbol{y}^i \end{array}\right] = \left[\begin{array}{cc} \eta_0 \bar{\boldsymbol{T}}_0 & -\bar{\boldsymbol{K}}_0 \\ \eta_0\eta_1 \bar{\boldsymbol{K}}_0 & \eta_1 \bar{\boldsymbol{T}}_0 \end{array}\right] \cdot \left[\begin{array}{c} \boldsymbol{x}^i \\ \boldsymbol{y}^i \end{array}\right] - \left[\begin{array}{cc} \eta_1 \bar{\boldsymbol{T}}_1 & -\bar{\boldsymbol{K}}_1 \\ \eta_0\eta_1 \bar{\boldsymbol{K}}_1 & \eta_0 \bar{\boldsymbol{T}}_1 \end{array}\right] \cdot \left[\begin{array}{c} \boldsymbol{x}^i \\ \boldsymbol{y}^i \end{array}\right]. \tag{40}$$

When the contrast decreases to very low values, the RHS of S-CTF is vanishingly small, but it is obtained by the subtraction of two terms that are relatively large. Then, depending on the accuracy of the matrix-vector multiplications in (40), the RHS of S-CTF may not be calculated accurately when the contrast is very low.

In order to obtain a stable formulation for arbitrarily low contrasts, we rearrange the RHS of S-CTF by introducing fictitious incident fields [40], i.e.,

$$\boldsymbol{E}_f^i(\boldsymbol{r}) = \left[\boldsymbol{E}^i(\boldsymbol{r})\right]_{\substack{\epsilon_0 \to \epsilon_1 \\ \mu_0 \to \mu_1}} \tag{41}$$

$$\boldsymbol{H}_f^i(\boldsymbol{r}) = \left[\boldsymbol{H}^i(\boldsymbol{r})\right]_{\substack{\epsilon_0 \to \epsilon_1 \\ \mu_0 \to \mu_1}}. \tag{42}$$

Similar to (26), the fictitious incident fields satisfy

$$\left[\begin{array}{cc} \eta_1 \mathcal{T}_1 & -\mathcal{K}_1 + 0.5\mathcal{I}^{\times n} \\ \mathcal{K}_1 - 0.5\mathcal{I}^{\times n} & \eta_1^{-1} \mathcal{T}_1 \end{array}\right] \cdot \left[\begin{array}{c} \hat{\boldsymbol{n}} \times \boldsymbol{H}_f^i \\ -\hat{\boldsymbol{n}} \times \boldsymbol{E}_f^i \end{array}\right](\boldsymbol{r}) = \left[\begin{array}{c} 0 \\ 0 \end{array}\right]. \tag{43}$$

Using (43) in (27), we obtain

$$\begin{aligned} &\hat{\boldsymbol{t}} \cdot \left[\begin{array}{cc} \eta_0 \mathcal{T}_0 + \eta_1 \mathcal{T}_1 & -\Big(\mathcal{K}_0 + \mathcal{K}_1\Big) \\ \eta_0\eta_1 \Big(\mathcal{K}_0 + \mathcal{K}_1\Big) & \eta_1 \mathcal{T}_0 + \eta_0 \mathcal{T}_1 \end{array}\right] \cdot \left[\begin{array}{c} \boldsymbol{J}^r \\ \boldsymbol{M}^r \end{array}\right](\boldsymbol{r}) \\ &= -0.5\hat{\boldsymbol{t}} \cdot \left[\begin{array}{c} \boldsymbol{E}^i - \boldsymbol{E}_f^i \\ \eta_0\eta_1 \boldsymbol{H}^i - \eta_0\eta_1 \boldsymbol{H}_f^i \end{array}\right](\boldsymbol{r}) - \hat{\boldsymbol{t}} \cdot \left[\begin{array}{cc} \eta_1 \mathcal{T}_1 & -\mathcal{K}_1 \\ \eta_0\eta_1 \mathcal{K}_1 & \eta_0 \mathcal{T}_1 \end{array}\right] \cdot \left[\begin{array}{c} \hat{\boldsymbol{n}} \times \boldsymbol{H}^i - \hat{\boldsymbol{n}} \times \boldsymbol{H}_f^i \\ -\hat{\boldsymbol{n}} \times \boldsymbol{E}^i + \hat{\boldsymbol{n}} \times \boldsymbol{E}_f^i \end{array}\right](\boldsymbol{r}). \end{aligned} \tag{44}$$

which we call FBS-CTF. Discretization of FBS-CTF leads to

$$\left[\begin{array}{cc} \bar{\boldsymbol{Z}}_{11} & \bar{\boldsymbol{Z}}_{12} \\ \bar{\boldsymbol{Z}}_{21} & \bar{\boldsymbol{Z}}_{22} \end{array}\right] \cdot \left[\begin{array}{c} \boldsymbol{x}^r \\ \boldsymbol{y}^r \end{array}\right] = -0.5 \left[\begin{array}{cc} \bar{\boldsymbol{I}} & 0 \\ 0 & \bar{\boldsymbol{I}} \end{array}\right]^{-1} \cdot \left[\begin{array}{c} \boldsymbol{v}_f \\ \eta_0\eta_1 \boldsymbol{w}_f \end{array}\right] - \left[\begin{array}{cc} \eta_1 \bar{\boldsymbol{T}}_1 & -\bar{\boldsymbol{K}}_1 \\ \eta_0\eta_1 \bar{\boldsymbol{K}}_1 & \eta_0 \bar{\boldsymbol{T}}_1 \end{array}\right] \cdot \left[\begin{array}{cc} \bar{\boldsymbol{I}} & 0 \\ 0 & \bar{\boldsymbol{I}} \end{array}\right]^{-1} \cdot \left[\begin{array}{c} \boldsymbol{w}_f^{\times n} \\ -\boldsymbol{v}_f^{\times n} \end{array}\right], \tag{45}$$

where

$$\boldsymbol{v}_f[m] = \int_{A_m} d\boldsymbol{r} \boldsymbol{t}_m(\boldsymbol{r}) \cdot \big(\boldsymbol{E}^i(\boldsymbol{r}) - \boldsymbol{E}_f^i(\boldsymbol{r})\big) \tag{46}$$

$$\boldsymbol{w}_f[m] = \int_{A_m} d\boldsymbol{r} \boldsymbol{t}_m(\boldsymbol{r}) \cdot \big(\boldsymbol{H}^i(\boldsymbol{r}) - \boldsymbol{H}_f^i(\boldsymbol{r})\big) \tag{47}$$

$$\boldsymbol{v}_f^{\times n}[m] = \int_{A_m} d\boldsymbol{r} \boldsymbol{t}_m(\boldsymbol{r}) \cdot \hat{\boldsymbol{n}} \times \big(\boldsymbol{E}^i(\boldsymbol{r}) - \boldsymbol{E}_f^i(\boldsymbol{r})\big) \tag{48}$$

$$\boldsymbol{w}_f^{\times n}[m] = \int_{A_m} d\boldsymbol{r} \boldsymbol{t}_m(\boldsymbol{r}) \cdot \hat{\boldsymbol{n}} \times \big(\boldsymbol{H}^i(\boldsymbol{r}) - \boldsymbol{H}_f^i(\boldsymbol{r})\big). \tag{49}$$

In (46)–(49), real and fictitious incident fields are subtracted from each other analytically in the continuous space before the discretization. Then, the RHS of FBS-CTF in (45) is obtained as the sum of two terms, which are both small when the contrast is low, and it can be calculated accurately for arbitrarily low contrasts. FBS-CTF can easily be obtained from the conventional CTF implementation and its extra cost is negligible.

5. RESULTS

In order to demonstrate the accuracy of FBS-CTF compared to CTF and S-CTF for arbitrarily low contrasts, we consider the solution of scattering problems involving a sphere of radius $0.5\lambda_0$, where λ_0 is the wavelength outside the sphere. The sphere is located in free space and illuminated by a plane wave propagating in the z direction with the electric field polarized in the x direction. Discretization of the sphere with $\lambda_0/10$ mesh size leads to matrix equations with 1860 unknowns. Matrix elements are computed directly with 5×10^{-3} relative error. Fig. 1 depicts the bistatic radar cross section (RCS), when the relative permittivity of the sphere is 1.1, $1.0 + 10^{-3}$, $1.0 + 10^{-6}$, and $1.0 + 10^{-9}$. With these values, the contrast of the sphere, i.e., $(\epsilon_1 - \epsilon_0)/\epsilon_0$, changes from 0.1 to 10^{-9}. Normalized RCS (RCS/λ_1^2) is plotted in decibels (dB) as a function of the observation angle on the $\phi = 0^\circ$ plane, where 0° corresponds to the forward-scattering direction. RCS values are also computed analytically by a Mie-series solution. Fig. 1(a) shows that CTF, S-CTF, and FBS-CTF provide accurate results when the contrast is 0.1. As the contrast decreases to 10^{-3} and 10^{-6}, however, CTF breaks down and cannot provide accurate results. When the contrast is further reduced to 10^{-9}, S-CTF also fails to agree with the analytical solution. On the other hand, FBS-CTF provides accurate results for all contrast in Fig. 1.

Fig. 2 presents the RCS of the sphere with radius $0.5\lambda_0$, when the contrast is 10^{-6} and 10^{-9}. This time, the scattering problems are solved iteratively, where the far-field interactions are computed via FMM with two digits of accuracy. Fig. 2(a) shows that the FMM solution of S-CTF is significantly inaccurate when the contrast is 10^{-6}, as opposed to the MOM solution in Fig. 2(c). This is because the accuracy of S-CTF is sensitive to the accuracy of the matrix-vector multiplications when the contrast is very low. However, as demonstrated in Fig. 2, FBS-CTF is stable for arbitrarily low contrasts, even with finite-precision methods.

Fig. 3 presents the solution of large scattering problems, involving a sphere of radius $6\lambda_0$. The sphere is again located in free space and illuminated by a plane wave propagating in the z direction with the electric field polarized in the x direction. Discretization of the sphere with $\lambda_0/10$ mesh size leads to matrix equations with 264,006 unknowns. Scattering problems are solved iteratively via MLFMA with two digits of accuracy. Figs. 3(a) and 3(b) present the bistatic RCS values on the $\phi = 0^\circ$ plane

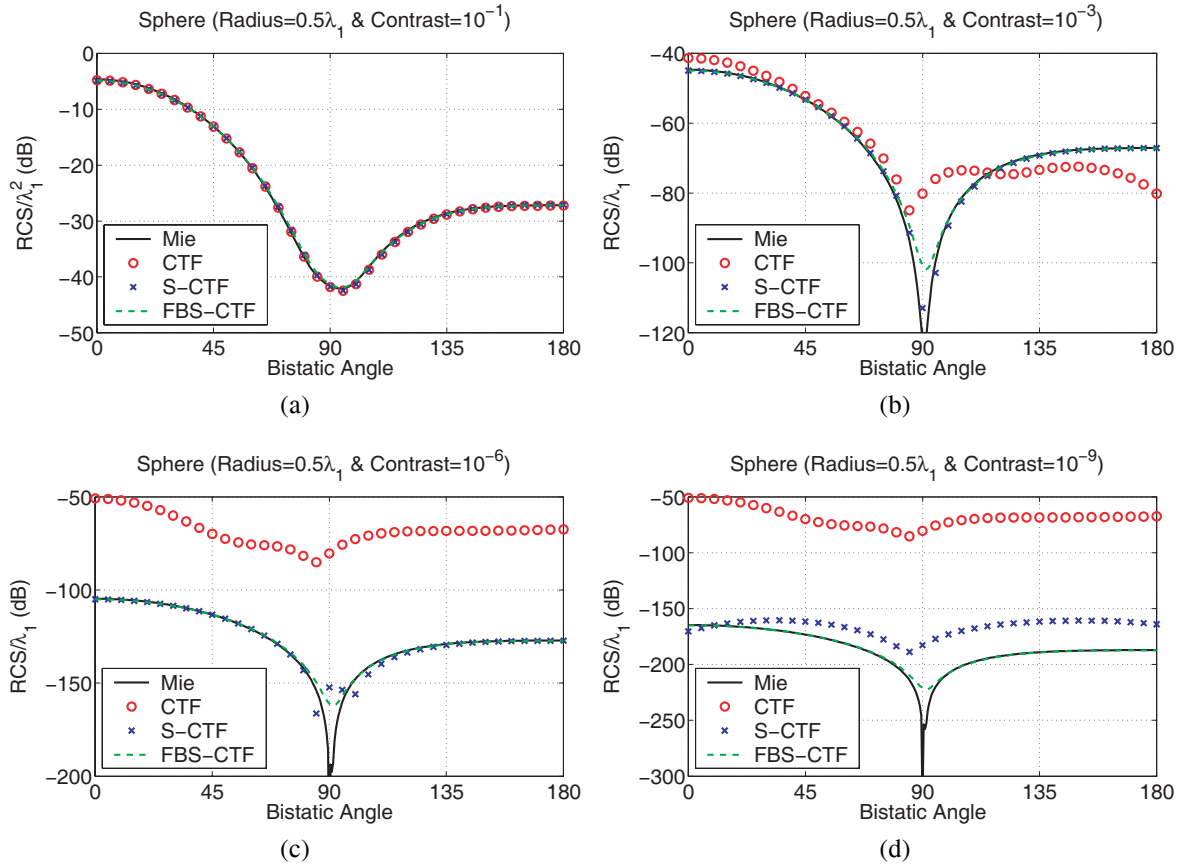

Fig. 1. Normalized bistatic RCS (RCS/λ_0^2 on the $\phi = 0^\circ$ plane) of a sphere of radius $0.5\lambda_0$, where λ_0 is the wavelength outside the sphere (free space), when the relative permittivity of the sphere is (a) $1 + 10^{-1}$, (b) $1 + 10^{-3}$, (b) $1 + 10^{-6}$, and (c) $1 + 10^{-9}$. The sphere is illuminated by a plane wave propagating in the z direction with the electric field polarized in the x direction.

when the contrast of the sphere is 10^{-3} and 10^{-6}, respectively. Similar to the previous examples, CTF is significantly inaccurate in both cases. When the contrast is 10^{-6}, RCS values obtained with S-CTF are also inaccurate and inconsistent with the analytical results, especially in the back-scattering direction. On the other hand, FBS-CTF provides accurate results for both 10^{-3} and 10^{-6} contrasts. RCS values provided by this formulation deviate from the analytical results only around 90°, where scattering is very low.

Finally, Fig. 4 presents the results of scattering problems involving a $\lambda_0 \times \lambda_0 \times \lambda_0/10$ dielectric slab, where $\lambda_0 = 1$ m is the wavelength outside the object (free space). The slab is located at the origin as depicted in the inset of Fig 4(a), and it is illuminated by a plane wave propagating in the z direction with the electric field polarized in the x direction. We consider four different relative permittivities for the slab, i.e., 2.0, 1.1, $1 + 10^{-3}$, and $1 + 10^{-6}$, corresponding to 1.0, 0.1, 10^{-3}, and 10^{-6} contrasts, respectively. The slab is discretized with $\lambda_0/20$ mesh size leading to matrix equations with 11,424 unknowns. Scattering problems are solved by using FMM, where the near-field interactions are calculated with 5×10^{-3} error and the far-field interactions are calculated with two digits of accuracy. We plot the bistatic RCS in dBms as a function of the observation angle on the $\phi = 0^\circ$ plane. RCS values obtained by using CTF and FBS-CTF are compared with those obtained by using the electric-field VIE [21], which is immune to low-contrast problems. As depicted in Fig. 4(a), CTF and FBS-CTF are consistent with VIE when the contrast of the slab is relatively large (1.0). As the contrast decreases to 0.1, 10^{-3}, 10^{-6}, however, RCS values obtained with CTF

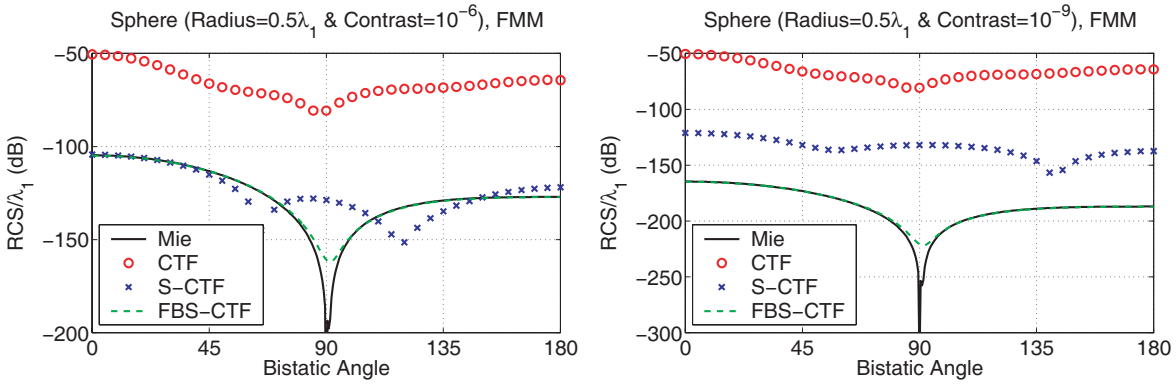

Fig. 2. Normalized bistatic RCS (RCS/λ_0^2 on the $\phi = 0^\circ$ plane) of a sphere of radius $0.5\lambda_0$, where λ_0 is the wavelength outside the sphere (free space), when the relative permittivity of the sphere is (a) $1 + 10^{-6}$ and (b) $1 + 10^{-9}$. Scattering problems are solved iteratively by using FMM.

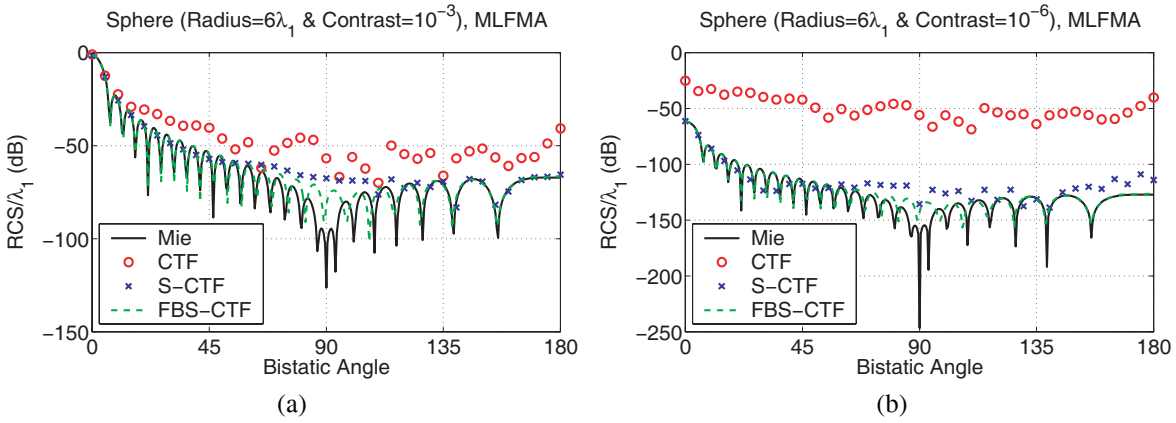

Fig. 3. Normalized bistatic RCS (RCS/λ_0^2 on the $\phi = 0^\circ$ plane) of a sphere of radius $6\lambda_0$, where λ_0 is the wavelength outside the sphere (free space), when the relative permittivity of the sphere is (a) $1 + 10^{-3}$ and (b) $1 + 10^{-6}$. Scattering problems are solved iteratively by using MLFMA.

become inconsistent with the values obtained with FBS-CTF and VIE. As in the previous examples, FBS-CTF is accurate and agrees well with the reference VIE for all contrasts.

6. CONCLUSION

We present a robust stabilization technique for the accurate surface formulations of dielectric bodies with arbitrarily low contrasts. The technique is based on extracting the nonradiating currents, using fictitious incident fields to rearrange the RHSs of the equations, and solving the modified equations to obtain the radiating currents very accurately. The stabilization is easy to implement by modifying the existing codes for the conventional formulations, and its computational cost is negligible. We apply the stabilization procedure to CTF, resulting in a stable formulation called FBS-CTF, which provides accurate results even for extremely low-contrast objects.

REFERENCES

[1] C. Müller, *Foundations of the Mathematical Theory of Electromagnetic Waves*. New York: Springer, 1969.

[2] A. J. Poggio and E. K. Miller, "Integral equation solutions of three-dimensional scattering problems," in *Computer Techniques for Electromagnetics*, R. Mittra, Ed. Oxford: Pergamon Press, 1973, Chap. 4.

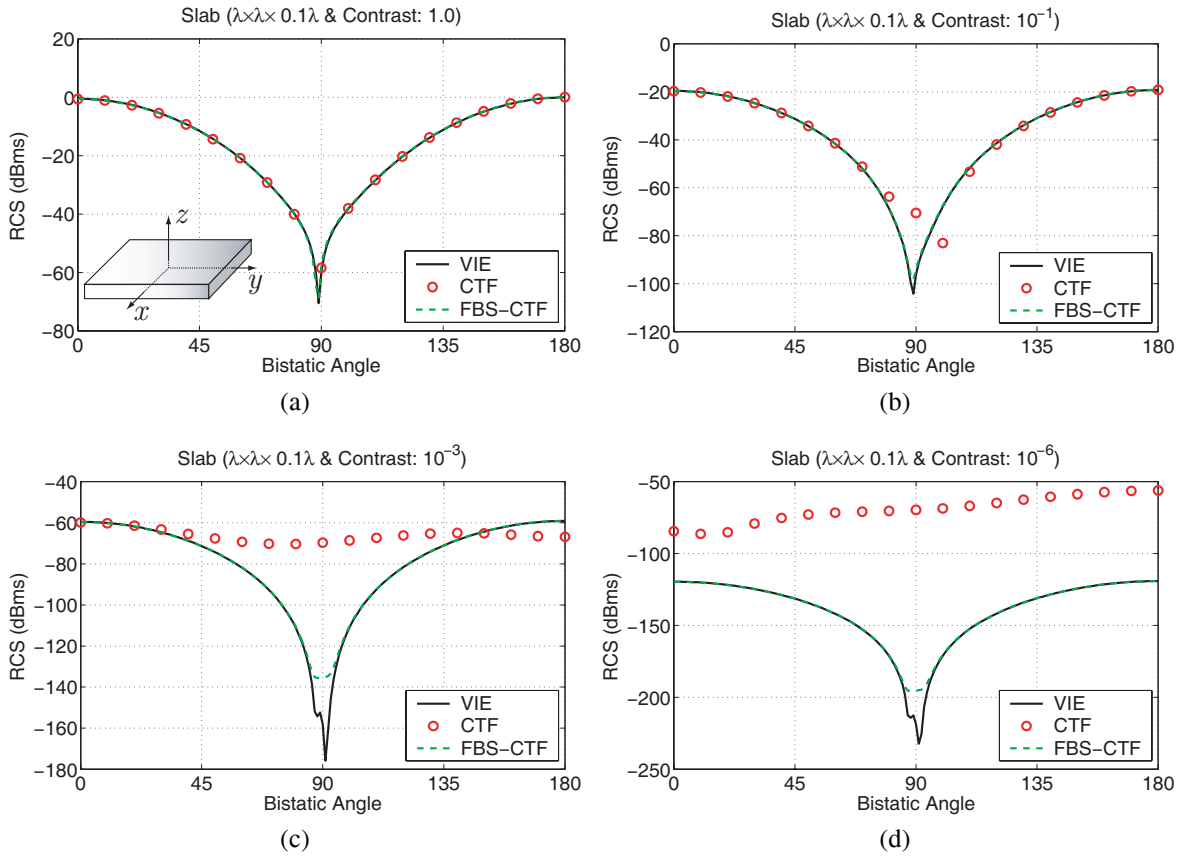

Fig. 4. Bistatic RCS (dBm^2) of a $\lambda_0 \times \lambda_0 \times \lambda_0/10$ slab, where $\lambda_0 = 1$ m is the wavelength outside the slab (free space), when the relative permittivity of the sphere is (a) 2.0, (b) 1.1, (c) $1 + 10^{-3}$, and (d) $1 + 10^{-6}$. The slab is illuminated by a plane wave propagating in the z direction with the electric field polarized in the x direction, and the RCS values are plotted on the $\phi = 0^\circ$ plane.

[3] T. K. Wu and L. L. Tsai, "Scattering from arbitrarily-shaped lossy dielectric bodies of revolution," *Radio Sci.*, vol. 12, pp. 709–718, Sep.-Oct. 1977.

[4] Y. Chang and R. F. Harrington, "A surface formulation for characteristic modes of material bodies," *IEEE Trans. Antennas Propagat.*, vol. AP-25, pp. 789–795, Nov. 1977.

[5] J. R. Mautz and R. F. Harrington, "Electromagnetic scattering from a homogeneous material body of revolution," *AEÜ*, vol. 33, pp. 71–80, Feb. 1979.

[6] R. F. Harrington, "Boundary integral formulations for homogeneous material bodies," *J. Electromagn. Waves Applicat.*, vol. 3, no. 1, pp. 1–15, 1989.

[7] S. M. Rao and D. R. Wilton, "E-field, H-field, and combined field solution for arbitrarily shaped three-dimensional dielectric bodies," *Electromagn.*, vol. 10, no. 4, pp. 407–421, Oct.-Dec. 1990.

[8] X.-Q. Sheng, J.-M. Jin, J. Song, W. C. Chew, and C.-C. Lu, "Solution of combined-field integral equation using multilevel fast multipole algorithm for scattering by homogeneous bodies," *IEEE Trans. Antennas Propagat.*, vol. 46, no. 11, pp. 1718–1726, Nov. 1998.

[9] P. Ylä-Oijala, "Application of a novel CFIE for electromagnetic scattering by dielectric objects," *Microwave and Opt. Technol.*, vol. 35, no. 10, pp. 3–5, Oct. 2002.

[10] K. C. Donepudi, J.-M. Jin, and W. C. Chew, "A higher order multilevel fast multipole algorithm for scattering from mixed conducting/dielectric bodies," *IEEE Trans. Antennas Propag.*, vol. 51, no. 10, pp. 2814–2821, Oct. 2003.

[11] T. W. Lloyd, J. M. Song, and M. Yang, "Numerical study of surface integral formulations for low-contrast objects," *IEEE Antennas Wireless Propagat. Lett.*, vol. 4, pp. 482–485, 2005.

[12] P. Ylä-Oijala and M. Taskinen, "Application of combined field integral equation for electromagnetic

scattering by dielectric and composite objects," *IEEE Trans. Antennas Propagat.*, vol. 53, no. 3, pp. 1168–1173, Mar. 2005.

[13] P. Ylä-Oijala, M. Taskinen, and S. Järvenpää, "Surface integral equation formulations for solving electromagnetic scattering problems with iterative methods," *Radio Science*, vol. 40, RS6002, doi:10.1029/2004RS003169, Nov. 2005.

[14] P. Ylä-Oijala and M. Taskinen, "Well-conditioned Müller formulation for electromagnetic scattering by dielectric objects," *IEEE Trans. Antennas Propagat.*, vol. 53, no. 10, pp. 3316–3323, Oct. 2005.

[15] P. Ylä-Oijala and M. Taskinen, "Improving conditioning of electromagnetic surface integral equations using normalized field quantities," *IEEE Trans. Antennas Propagat.*, vol. 55, no. 1, pp. 178–185, Jan. 2007.

[16] M. Hammer, D. Schweitzer, B. Michel, E. Thamm, and A. Kolb, "Single scattering by red blood cells," *Appl. Optics*, vol. 37, no. 31, pp. 7410–7418, Nov. 1998.

[17] J. Q. Lu, P. Yang, and X.-H. Hu, "Simulations of light scattering from a biconcave red blood cell using the finite-difference time-domain method," *J. Biomed. Opt.*, vol. 10(2), no. 024022, March/Apr. 2005.

[18] D. A. Hill, "Electromagnetic scattering by buried objects of low contrast," *IEEE Trans. Geosci. Remote Sen.*, vol. 26, no. 2, pp. 195–203, Mar. 1988.

[19] E. S. Thiele, "Scattering of electromagnetic radiation by complex microstructures in the resonant regime," Ph.D. thesis, University of Pennsylvania, 1998.

[20] P. Loschialpo, D. W. Forester, and J. Schelleng, "Anomalous transmission through near unit index contrast dielectric photonic crystals," *J. Appl. Phys.*, vol. 86, no. 10, pp. 5342–5347, Nov. 1999.

[21] D. H. Schaubert, D. R. Wilton, and A. W. Glisson, "A tedrahedral modeling method for electromagnetic scattering by arbitrarily shaped inhomogeneous dielectric bodies," *IEEE Trans. Antennas Propagat.*, vol. AP-32, no. 1, pp. 77–85, Jan. 1984.

[22] P. M. Goggans and A. Glisson, "A surface integral equation formulation for low contrast scatterers based on radiation currents," *ACES Journal*, vol. 10, pp. 15–18, Mar. 1995.

[23] Ö. Ergül and L. Gürel, "Stabilization of integral-equation formulations for the accurate solution of scattering problems involving low-contrast dielectric objects," *IEEE Trans. Antennas Propagat.*, vol. 56, no. 3, pp. 799–805, Mar. 2008.

[24] R. Coifman, V. Rokhlin, and S. Wandzura, "The fast multipole method for the wave equation: a pedestrian prescription," *IEEE Ant. Propag. Mag.*, vol. 35, no. 3, pp. 7–12, Jun. 1993.

[25] J. Song, C.-C. Lu, and W. C. Chew, "Multilevel fast multipole algorithm for electromagnetic scattering by large complex objects," *IEEE Trans. Antennas Propagat.*, vol. 45, no. 10, pp. 1488–1493, Oct. 1997.

[26] P. Ylä-Oijala, "Numerical analysis of combined field integral equation formulations for electromagnetic scattering by dielectric and composite objects," *Progress in Electromagnetics Research C,* vol. 3, pp. 19–43, 2008.

[27] P. Ylä-Oijala, M. Taskinen, and S. Järvenpää, "Analysis of surface integral equations in electromagnetic scattering and radiation problems," *Engineering Analysis with Boundary Elements*, vol. 32, no. 3, pp. 196–209, Mar. 2008.

[28] Ö. Ergül and L. Gürel, "Fast and accurate solutions of scattering problems involving dielectric objects with moderate and low contrasts," in *Proc. 2007 Computational Electromagnetics Workshop*, 2007, pp. 59–64.

[29] Ö. Ergül and L. Gürel, "Comparison of integral-equation formulations for the fast and accurate solution of scattering problems involving dielectric objects with the multilevel fast multipole algorithm," *IEEE Trans. Antennas Propag.*, submitted for publication.

[30] S. M. Rao, D. R. Wilton, and A. W. Glisson, "Electromagnetic scattering by surfaces of arbitrary shape," *IEEE Trans. Antennas Propagat.*, vol. AP-30, no. 3, pp. 409–418, May 1982.

[31] Ö. Ergül and L. Gürel, "Linear-linear basis functions for MLFMA solutions of magnetic-field and combined-field integral equations," *IEEE Trans. Antennas Propagat.*, vol. 55, no. 4, pp. 1103–1110, Apr. 2007.

[32] D. A. Dunavant, "High degree efficient symmetrical Gaussian quadrature rules for the triangle," *Int. J. Numer. Meth. Eng.*, vol. 21, pp. 1129–1148, 1985.

[33] R. D. Graglia, "On the numerical integration of the linear shape functions times the 3-D Green's function or its gradient on a plane triangle," *IEEE Trans. Antennas Propagat.*, vol. 41, no. 10, pp. 1448–1455, Oct. 1993.

[34] R. E. Hodges and Y. Rahmat-Samii, "The evaluation of MFIE integrals with the use of vector triangle basis functions," *Microwave Opt. Technol. Lett.*, vol. 14, no. 1, pp. 9–14, Jan. 1997.

[35] Ö. Ergül, "Fast multipole method for the solution of electromagnetic scattering problems," M.S. thesis, Bilkent University, Ankara, Turkey, Jun. 2003.

[36] P. Y.-Oijala and M. Taskinen, "Calculation of CFIE impedance matrix elements with RWG and $\hat{\boldsymbol{n}}\times$RWG functions," *IEEE Trans. Antennas Propagat.*, vol. 51, no. 8, pp. 1837–1846, Aug. 2003.

[37] L. Gürel and Ö. Ergül, "Singularity of the magnetic-field integral equation and its extraction," *IEEE Antennas Wireless Propagat. Lett.*, vol. 4, pp. 229–232, 2005.

[38] W. C. Chew, J.-M. Jin, E. Michielssen, and J. Song, *Fast and Efficient Algorithms in Computational Electromagnetics*. Boston, MA: Artech House, 2001.

[39] S. Koc, J. M. Song, and W. C. Chew, "Error analysis for the numerical evaluation of the diagonal forms of the scalar spherical addition theorem," *SIAM J. Numer. Anal.*, vol. 36, no. 3, pp. 906–921, 1999.

[40] Ö. Ergül and L. Gürel, "Novel electromagnetic surface integral equations for highly accurate computations of dielectric bodies with arbitrarily low contrasts," *Journal of Computational Physics*, doi:10.1016/j.jcp.2008.08.004, 2008.